Geophysical Journal International

Geophys. J. Int. (2013) **195,** 650–660
Advance Access publication 2013 July 25

doi: 10.1093/gji/ggt254

The 2011 M_W 6.8 Burma earthquake: fault constraints provided by multiple SAR techniques

Wanpeng Feng,[1,2] Zhenhong Li,[1] John R. Elliott,[3] Yo Fukushima,[4] Trevor Hoey,[1] Andrew Singleton,[1] Robert Cook[1] and Zhonghuai Xu[2]

[1]*COMET+, School of Geographical and Earth Sciences, University of Glasgow, Glasgow G*12 8*QQ, UK. E-mail: w.feng.1@research.gla.ac.uk*
[2]*Institute of Geophysics, China Earthquake Administration, Beijing, China*
[3]*COMET+, Department of Earth Sciences, University of Oxford, Parks Road, Oxford, UK*
[4]*Disaster Prevention Research Institute, Kyoto University,* 611-0011 *Gokasho, Uji, Kyoto, Japan*

Accepted 2013 June 25. Received 2013 June 25; in original form 2012 June 8

SUMMARY

We used two tracks of ALOS PALSAR images to investigate the focal mechanism and slip distribution of the 2011 March 24, M_W 6.8 Burma strike-slip earthquake. Three different SAR techniques, namely conventional interferometry, SAR pixel offsets (SPO) and multiple-aperture InSAR (MAI), were employed to obtain the coseismic surface deformation fields along the ∼30 km length of the fault rupture. Along-track measurements from SPO and MAI techniques show a high correlation, and were subsequently used to precisely determine the location and extent of the surface fault trace. The best-fitting fault model geometry derived from an iterative inversion technique suggests that the rupture occurred on a near-vertical sinistral strike-slip fault west of the Nam Ma fault with a strike of 70°. A maximum slip of 4.2 m occurs at a depth of 2.5 km, with significant slip constrained only to the upper 10 km of the crust.

Key words: Numerical solutions; Inverse theory; Radar interferometry; Seismicity and tectonics.

1 INTRODUCTION

On 2011 March 24th (UTC Time 13:55:12), a M_W 6.8 earthquake struck Shan state in Eastern Burma (Myanmar) (Trisirisatayawong *et al.* 2011), close to the border with Thailand and Laos (Fig. 1). The earthquake caused at least 70 fatalities, hundreds of injuries and several hundred building collapses, followed by landslides and other secondary hazards (Daneill *et al.* 2011). Moment tensor solutions from the USGS indicate a pure strike-slip rupture on a nearly vertical dipping fault, with an epicentre at (20.687°N, 99.822°E). In the past 30 yr, more than 40 $M > 5$ earthquakes have occurred in the vicinity of the Burma shear zone, all having similar strike-slip mechanisms (Fig. 1a). The 2011 Burma event was the largest shallow earthquake in this region for the past 50 yr. This region is affected by the north–south converging India-Asia collision and the eastward East Asia continental extrusion (Molnar & Tapponnier 1975; Yin 2000; Chung *et al.* 2005; Taylor & Yin 2009; Styron *et al.* 2010). The Sagaing fault is formed as a result of the oblique convergence between India and the Sunda plate, bisecting Burma from South to North, and accommodating the major dextral slip at a rate of 10–23 mm yr^{-1} (Maung 1987; Vigny *et al.* 2003; Socquet *et al.* 2006; Maurin *et al.* 2010; Wang *et al.* 2011a). All geological surveys, GPS observations and numerical simulations suggest that the slip rate of the Sagaing fault is about four times greater than that of the right-lateral Red River Fault (RRF) in Yunnan, China (the latter being approximately 2.5–5 mm yr^{-1}) (Scharer *et al.* 1990; Replumaz *et al.* 2001; Shen *et al.* 2005; Wang *et al.* 2011a). These two major strike-slip faults control the internal deformation within the Burma region. A set of nearly parallel ENE left-lateral faults (red lines in Fig. 1a) distributed in this area appear to be related to the clockwise rotation due to the dextral movements on the boundary (Fig. 1a) (Tapponnier & Molnar 1976; Taylor & Yin 2009). Among these strike-slip faults, the active Nam Ma fault (NMF) (which is probably a eastward extension of the fault associated with the 2011 Burma earthquake), extends in a NNE direction from the City of Mong Hpayak.

To improve our understanding of the nature of faulting in this region, we used a variety of SAR techniques, namely conventional differential interferometry, SAR pixel offsets (SPO), and multiple-aperture interferometry (MAI) to process two tracks of ALOS PALSAR images. From these we determined the fault trace for the Burma earthquake, and modelled its slip distribution using interferometric radar measurements of surface displacements.

2 COSEISMIC OBSERVATIONS FROM SAR DATA

To obtain precise coseismic surface displacements of the 2011 Burma earthquake, both ascending and descending tracks of L-band

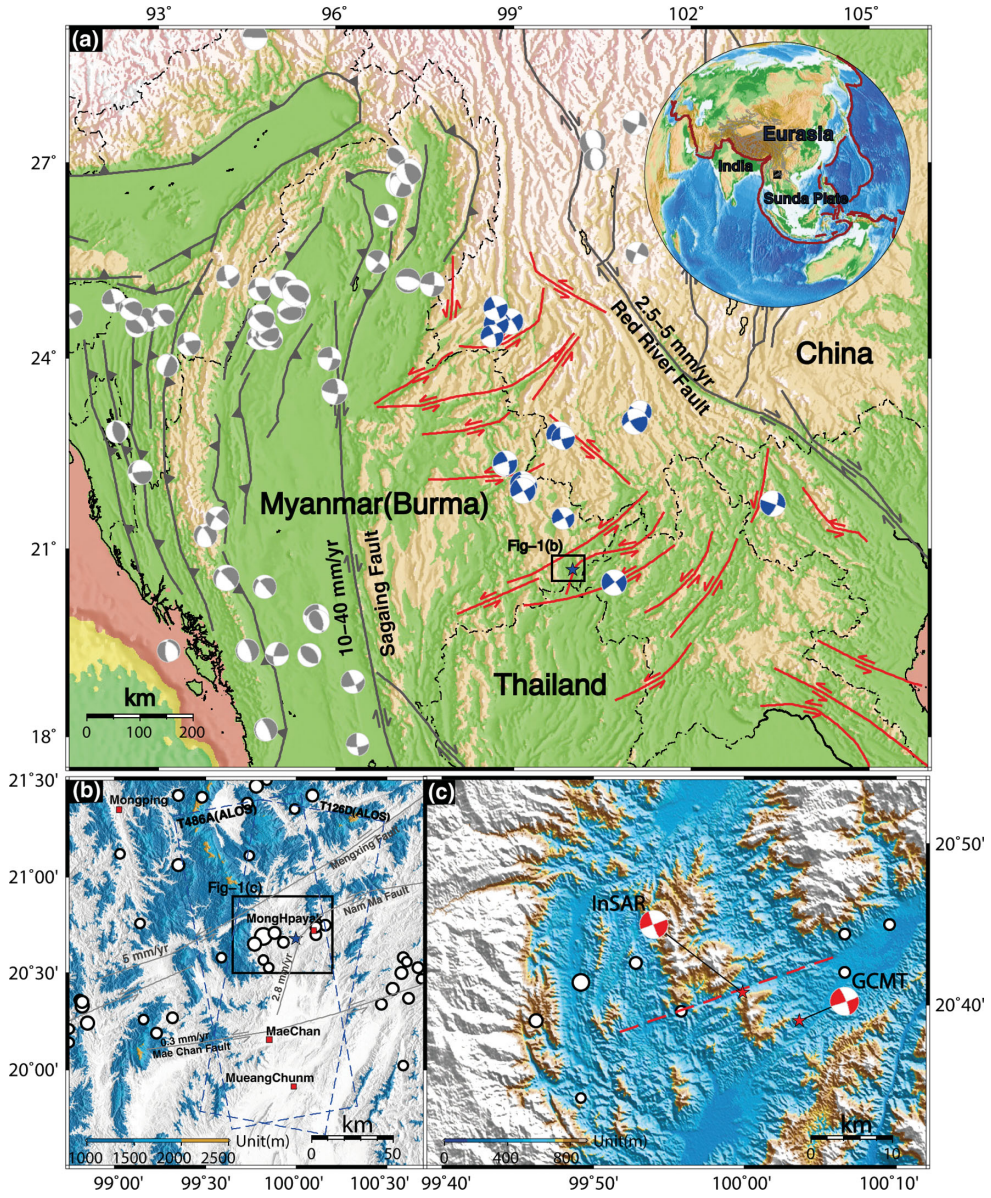

Figure 1. Tectonic setting of the Burma region. (a) Distribution of active faults (Styron *et al.* 2010). The focal mechanisms are obtained from the Global Centroid Moment Tensors (GCMT) database. Blue beach balls represent the basic characteristics of earthquakes (mainly strike-slip) in the research area, while grey ones indicate historic earthquakes of various types in its surrounding region. (b) The location of the 2011 Burma M_W 6.8 Earthquake (denoted by a blue star in (a)) and historic earthquake records (denoted by open circles). Blue dashed frames represent the spatial coverage of the ALOS images from tracks T126A and T486D. The black rectangle suggests the spatial coverage of (c). (c) SRTM shaded relief map of the earthquake area. The red line is the trace of the surface rupture determined from the SPO with ALOS PALSAR images.

ALOS PALSAR images (Table 1) were analysed using three different techniques: conventional differential interferometry, MAI and SPO.

2.1 Conventional InSAR

Two coseismic interferograms were formed from ALOS PALSAR images using the JPL/Caltech ROI_PAC software (version 3.1 beta) (Rosen *et al.* 2004). The topographic phase contribution was removed using version 4.1 of the Shuttle Radar Topography Mission (SRTM) 3-arcsecond (∼90 m) spacing digital elevation model (DEM) that has the voids filled from other data sources (Jarvis *et al.* 2008). The interferograms were first multilooked using factors of 2 and 8 in the range and azimuth directions, respectively, and then filtered by a Goldstein filter (Goldstein & Werner 1998) with a fast Fourier transformation (FFT) window of 128 × 128 pixels. Finally, the interferograms were unwrapped using the branch-cut algorithm (Goldstein *et al.* 1988) to obtain line-of-sight (LOS) displacements.

Fig. 2 shows different fringe patterns in the two ALOS interferograms because of their different radar LOS vectors (Table 1). The displacements along the range direction derived from descending track 126 (Fig. 2b) display an opposite sign compared with those from the ascending track 486 (Fig. 2f). In both ascending and descending interferograms, the number of fringes on both sides of the faults are similar (Figs 2a and e), suggesting that this event is associated with a steeply-dipping WSW-ENE strike-slipping fault with a limited amount of dip-slip displacements.

Table 1. ALOS PALSAR images used in this study.

Mode	Track	Master (YYYY-MM-DD)	Slave (YYYY-MM-DD)	Baseline[a] (m)	LOS Vector[b] East, North, Up	Days between the earthquake and postseismic image	stddev[c] (mm)	Stddev[d] (mm)
Descending	126	2011-02-14	2011-04-01	460	[0.6412, −0.1404,0.7543]	8	6.5	13.1
Ascending	486	2011-02-16	2011-04-03	30	[−0.5866, −0.1290,0.7995]	10	4.3	12.5

[a]Perpendicular baseline in the centre of the image.
[b]The unit vector [d_e, d_n, d_u] of the radar line of sight.
[c]Standard deviations calculated using all valid points in the non-deforming area (Figs S4b and e).
[d]Standard deviations calculated using all the valid points in residual interferograms (Figs 6c and f).

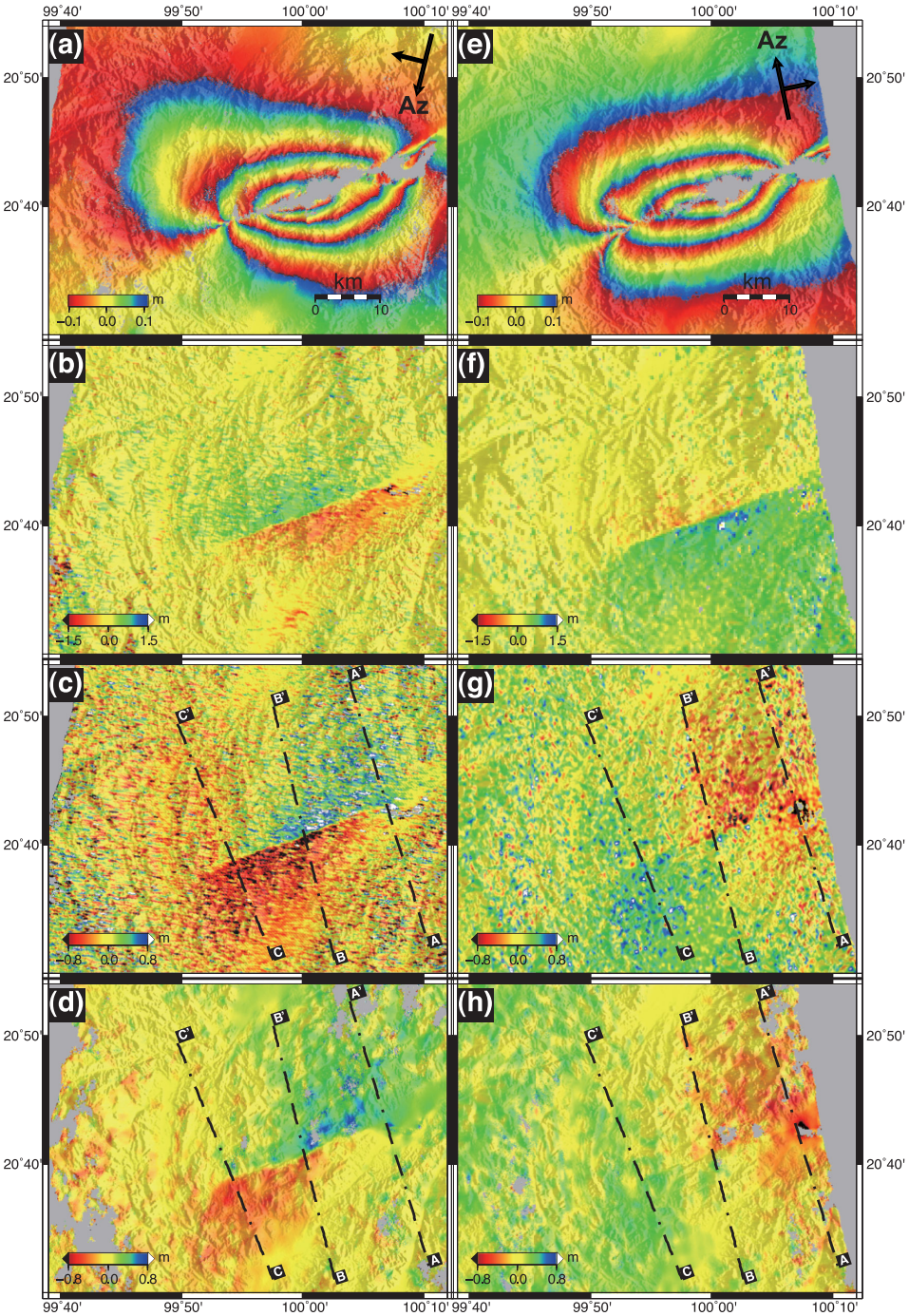

Figure 2. Coseismic observations obtained from descending ALOS track 126 (a, b, c, d) and ascending ALOS track 486 (e, f, g, h) by different processing methods. (a) and (e) are formed by conventional interferometry and re-wrapped with an interval of −0.1 and 0.1 m; (b) and (f) are range offsets, while (c) and (g) are azimuth offsets. (d) and (h) are MAI maps. Profiles A–C are shown in Fig. 3.

2.2 MAI

A major limitation of conventional InSAR is that it only provides one-dimensional displacements along the radar light-of-sight (LOS), which is the projection of the three components of actual surface displacements associated with geophysical events. Considering the difference between results from the backward part and forward part of signals, a second dimension (along-track) of deformation from one interferometric pair can be measured by a split-beam technique (Bechor & Zebker 2006). In this study, we employed the open-source codes developed by Barbot *et al.* (2008) to generate along-track interferograms. Note that the detectable along-track displacement is in the range of $[-L/4, L/4]$ (where L is the antenna length and about 8.9 m for ALOS) and no phase unwrapping is required (Barbot *et al.* 2008). It is also worth pointing out that Barbot *et al.* (2008) applied a bandpass filter to the already focused SLC image to separate it into forward- and backward-looking scenes, reporting a 10 cm precision on their MAI results. On the contrary, the radar beam is split into two parts by restricting the azimuth resolution and the forward-/backward-looking scenes are focused in the other two studies (Bechor & Zebker 2006; Jung *et al.* 2009; Ben-Dov & Herring 2011), though the former with a deskewed geometry and the latter with a skewed geometry. Bechor & Zebker (2006) suggested the precision of their MAI results ranged from 5 to 8.8 cm depending on coherence, while Jung *et al.* (2009) found precision from 10.2 to 13.1 cm on their implementation.

Because the signal-noise ratio (SNR) of MAI interferograms is usually lower than that produced by conventional InSAR (Sun *et al.* 2008), stronger Goldstein filtering has been employed in MAI processing than that in conventional InSAR. The along-track displacements are shown in Figs 2(d) and (h), from which the rupture traces can be clearly observed. Formal errors of the MAI displacement maps were calculated using a small window of 4 × 4 pixels, and are about 0.08 m for both tracks.

2.3 SPO

To verify the reliability of along-track measurements from MAI, we also implemented SPO analysis (Michel *et al.* 1999), which has been widely used in previous studies (Fialko *et al.* 2001; Jónsson *et al.* 2002; Funning *et al.* 2005; Li *et al.* 2011). SPO analysis uses cross-correlation techniques and its accuracy depends on the characteristics of SAR images (e.g. pixel sizes and surface properties) (Michel *et al.* 1999). In this study, we utilized the *ampcor* program in the ROI_PAC package (Rosen *et al.* 2004) using a matching window of 128 × 128 pixels with the steps of 8 pixels in range and 24 pixels in azimuth to construct two range offset and two azimuth offset maps. We first chose a threshold of 2 m to remove points with a magnitude larger than the threshold (Pathier *et al.* 2006), and then applied a Gaussian smoothing filter, which is an iterative estimation for each pixel with a Gaussian operator of 7 × 7 pixels in the resultant offset maps.

With respect to the conventional interferograms, SPO maps include greater noise limiting their precision to 12–15 cm (Fialko *et al.* 2001; Jónsson *et al.* 2002), while MAI maps have smaller uncertainties in the level of 8 cm, even 2–4 cm in areas with coherence greater than 0.8 (Bechor & Zebker 2006). Figs 3(g) and (h) give the correlations between MAI and SPO displacements along the three profiles for both tracks 126 and 486. High-correlation coefficients are observed between the two data sets: 0.90 for track 126 and 0.87 for track 486, and their RMS differences are both 11.0 cm. This precision is consistent with those reported by previous studies (Barbot *et al.* 2008). Note that the fault trace can be clearly observed from both SPO and MAI maps (e.g. Figs 2b, c and f), but little can be seen on conventional interferograms due to the decorrelation caused by the surface ruptures (Figs 2a and e). The fault trace can be used to constrain earthquake models, but it was mainly used to validate our model in this study.

2.4 Data reduction and weighting

In order to minimize the computational task, the two interferograms and MAI maps are subsampled using the R-based method developed by Lohman & Simons (2005). Using the fault trace determined from both MAI and SPO maps (Fig. 2), we defined a simple near-vertical, strike-slip uniform fault plane to downsample of the two interferograms and MAI maps. The 620 and 608 points were obtained from tracks 126 and 486 interferograms (see Figs S6a and b), respectively, and 333 and 318 points from tracks 126 and 486 MAI displacements (Figs S6c and d), respectively.

For each conventional interferogram, we firstly calculated its experimental variogram with all valid points in the far field using a FFT method (Marcotte 1996) and then constructed a full variance-covariance matrix (VCM) using an exponential 1-D covariance function to quantify InSAR noises

$$C(r) = \sigma^2 e^{-\beta r}, \tag{1}$$

where σ^2 is the variance, r is the separation of the observations in kilometres and β determines the e-folding correlation length scale (Parsons *et al.* 2006). Variances of 80 and 45 mm^2 were observed for tracks 126 and 486, respectively, with a correlation length of ∼18 km for both tracks. It is clear that no clear directional signal can be seen in the 2-D variograms of both interferograms (Figs S4e and f). Furthermore, there is no clear sign of long-wavelength signals in either interferogram (Figs S4b and e). These suggest that ionospheric effects on both conventional interferograms are likely to be limited and can be neglected. Although the 486A MAI interferogram could be contaminated at the latitude of around 20.25° as seen in Fig. S5(h), the possible 'ionospheric zone' is far from the epicentre area and the magnitude of ionospheric delays is 0.05 m, that is, less than 6 per cent of the maximum azimuth coseismic measurements (0.8 m). On the other hand, the weights applied to the MAI data sets defined below are much smaller than other data sets. Therefore, the influence of ionospheric signals on the final slip solution should be minimal.

The use of a combination of different data sets in modelling requires the determination of the weighting of each data set. We firstly weighted each point using a small window as suggested by Simons *et al.* (2002) with the requirement that the sum of the normalized weight for each data set should be equal to unity. Secondly, relative weights were determined according to their variances in the far field: 0.45 for conventional InSAR datapoints and 0.025 for MAI datapoints (i.e. InSAR datapoints 18 times higher).

3 EARTHQUAKE MODELLING

A two-step inversion strategy is often employed to constrain the fault parameters with InSAR observations as performed in previous studies (Wright *et al.* 2003; Li *et al.* 2008; Atzori *et al.* 2009; Li *et al.* 2011). This comprises a nonlinear inversion to determine the fault geometry by minimizing the square misfit under the assumption of a uniform slip on a rectangular fault, followed by a linear inversion for estimating the slip distribution on the determined fault plane.

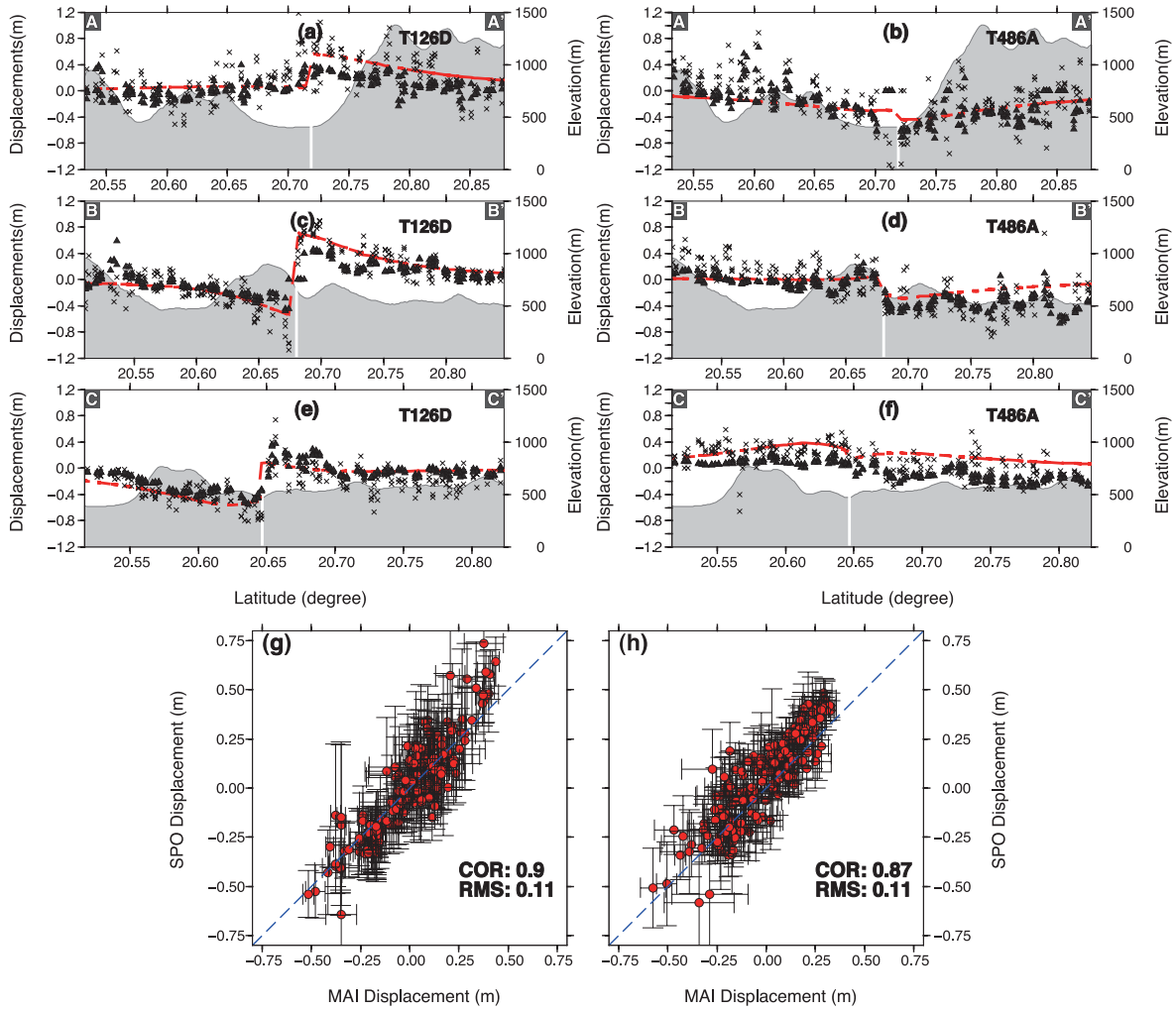

Figure 3. (a, c, e) Comparisons of the NNE-SSW profiles of A−A′, B−B′ and C−C′ from track 126D as shown in Fig. 2. Black triangles denote MAI measurements, while cross points represent SPO observations; (b), (d) and (f) are similar to (a), (c) and (e) but for track 486A. The grey-shaded region represents topography along each profile. The white lines down to the *x*-axis show the location of the seismic fault. The model displacements from the best-fitting slip distribution are shown as dashed red lines. (g) Comparison between SPO and MAI displacements for track 126D. The error bars denote 1σ of MAI measurements with a 4 × 4 pixels window size and 1σ of SPO. (h) similar to (g), but for track 486A.

However, the fault geometry determined under the assumption of a uniform slip is not necessarily the optimal one (especially the dip angle) for a spatially variable slip distribution (Burgmann *et al.* 2002; Fukahata & Wright 2008). In this paper, an iterative approach is presented to determine the optimal dip angle in the slip inversion.

In this study, multipeak particle swarm optimization (M-PSO) was employed for inverting fault geometry parameters including strike, dip, slip, length, top and bottom depth by minimizing the squared misfits between the observed and the predicted LOS displacements using a hybrid minimization algorithm (Feng & Li 2010). This algorithm has been successfully applied to several earthquakes (Li *et al.* 2008, 2011; Feng *et al.* 2009). Table 2 shows the best-fit uniform solution, of which the location, strike angle and the length of rupture are highly consistent with those derived directly from SPO and MAI maps as shown in Table 2 and the inverted dip has a difference of ∼7° compared with the GCMT solution.

Once the fault geometry is determined, the slip along the strike and dip direction show a linear relationship with surface displacements based on the classic theory of linear-elastic dislocation (Okada 1985). The fault location and strike determined in the previous step are consistent with SPO maps and MAI results, but the dip angle can be refined in the variable slip determination (Burgmann *et al.* 2002; Fukahata & Wright 2008). The relationship between observations and the slips at the patches can be written in the following form:

$$\begin{bmatrix} G_\delta \\ \alpha^2 L \end{bmatrix} S = \begin{bmatrix} D \\ 0 \end{bmatrix}, \tag{2}$$

where G_δ is the forward matrix (also called Green matrix) relating to the slip at the patches calculated by the Okada model (Okada 1985) for a given dip angle δ; Sis the slip vector at each patch and Dis the range change in the satellite LOS derived from InSAR measurements; L is the second-order finite difference operator (Jónsson *et al.* 2002) for estimating the roughness of the slip vector; α^2 is the weighting parameter, or smooth factor, in order to obtain the smoothest solution that does not degrade the fit to the observations. The bounded-variable least-squares algorithm (BVLS) (Stark & Parker 1992) was employed to solve the linear problems in this study with the slip of the elements on the left, right and bottom boundaries in the fault plane being set to zero.

During slip distribution inversions, the dip angle and smoothing factor (α^2) should be further optimized because those determined

Table 2. Fault geometry from seismic and geodetic sources.

Model[a]	Location		Focal			Length	Width	Depth[b]	M_W
	Lon	Lat	Strike	Dip	Rake	(km)	(km)	(km)	
USGS-BW	99.882	20.673	246	81	−3	–	–	8	6.7
GCMT	100.2	20.62	70	85	11	–	–	12.6	6.8
MAI/SPO[c]	99.795	20.89	70	–	–		–	–	–
Uniform Inv	99.995	20.674	69.7	92.7	1.8	22.4	8.4	4.6	6.8
Iterative Inv	99.995	20.674	69.7	88.3 ± 4	$4^d \pm 0.5$	60	20	10.0	6.8

[a]The models listed in the first column are from different sources: USGS-BW is derived from body wave data by USGS, GCMT is the Global CMT solution, 'Uniform Inv' is the uniform slip model, and 'Iterative Inv' is the refined model using the iterative method demonstrated in Section 3.3.
[b]The depth of GCMT solution is the centroid, while the depth of the Uniform Inversion (Uniform Inv) represents the centre of the fault plane.
[c]The geometry parameters of the fault were determined directly from the MAI/SPO maps.
[d]This is the average rake and its standard deviation calculated using all the rakes in the patches with a slip greater than 0.5 m.

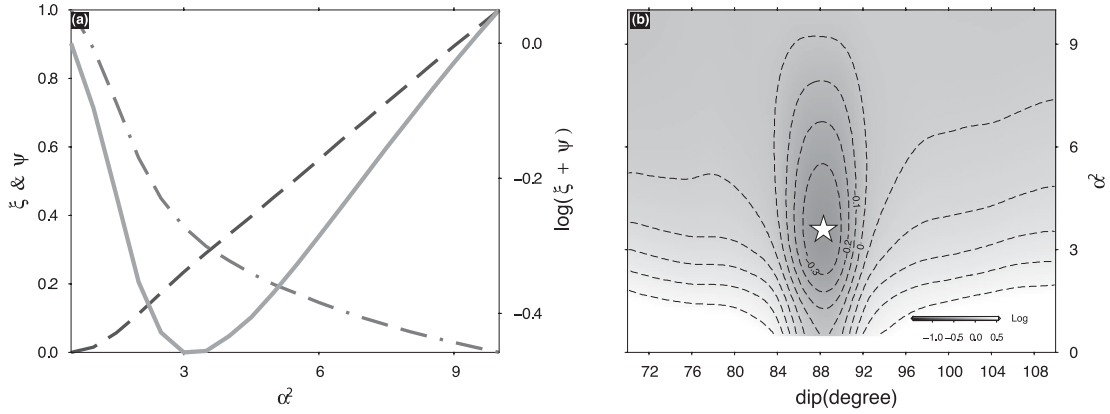

Figure 4. (a) A trade-off curve line associated with the model with a dip angle of 88.3°. The dashed and dash-dotted black lines show the trends of model roughness and the residuals of modelled simulations after normalizing ([ξ, ψ]), respectively, while the solid grey line represents log($\xi + \psi$). (b) Contour map of log($\xi + \psi$) with variations of dips and hyperparameters (α^2). White star indicates the point of global minimum.

under the assumption of uniform slips are not optimal for a spatially variable slip distribution (Burgmann *et al.* 2002). In this study, we firstly analysed the changing trends of the model roughness (ψ) and residuals (ξ) with the variation of smoothing weight at the given dip angle (Fig. 4a). The root-mean-square error was employed for estimating the residuals as defined here

$$\xi = \sqrt{(W(D - GS))^2 / N}, \tag{3}$$

where W is the weight matrix defined in the previous section (2.4) and N is the number of observations involved in the inversion. Meanwhile, the model roughness is the depiction of the result from smoothing the slip solution under the smooth factor as given by Jónsson *et al.* (2002)

$$\psi = \sum_{i=1}^{n} |p_i| / 2n, \tag{4}$$

where $p = LS$ and n is the number of subfaults. After normalization, the roughness curve line indicates a monotonic decreasing function, while the residual curve line implies a monotonic increasing function; it is hence impossible to retrieve a global minimum from both curve lines. To obtain the trade-off between the roughness (ψ) and residual (ξ), we built a Log-function $f(\delta, \alpha) = \log(\psi + \xi)$, which indicates a single minimum at $\alpha^2 \approx 4$ (grey solid line in Fig. 4a). To optimise both dip angle and α^2, the following four-step procedure was used in this study:

(a) estimate the solutions using BVLS with the variations of α^2 for a given dip angle. The fitting residuals (ξ) in the unit of metre and the model roughness (ψ) in the unit of metre per kilometre can be retrieved.

Note that the amplitude of α^2 is related to the definition of L in eq. (2). We set a series of α^2 in the range of [0.1,10] with an interval of 0.5.

(b) calculate ξ and ψ relating to a series of dips in the range of [80°, 100°] with an interval of 1° in an iterative way;

(c) normalize ξ and ψ using the following simple expression $(\{.\} - \min\{.\}) / (\max\{.\} - \min\{.\})$, where $\{.\}$ denotes the series of ξ and ψ. Note both variables become dimensionless.

(d) calculate $f(\delta, \alpha)$ for any given (δ, α) and plot f on a diagram as shown in Fig. 4(b), from which the optimal dip angle and smoothing operator can be directly determined.

The optimal dip angle and smoothing factor determined using the Log-function were directly employed to further develop the distributed slip model (model A). The uncertainty of slip solutions was calculated from 100 perturbed data sets that were created by adding simulated noise to the observations as proposed by Parsons *et al.* (2006). The standard deviation of slip at each patch is shown in Fig. 4.

Fig. 5(a) shows the optimal slip distribution of the 2011 Burma earthquake from both conventional InSAR and MAI observations (i.e. model A). The slip distribution is characterized by a peak

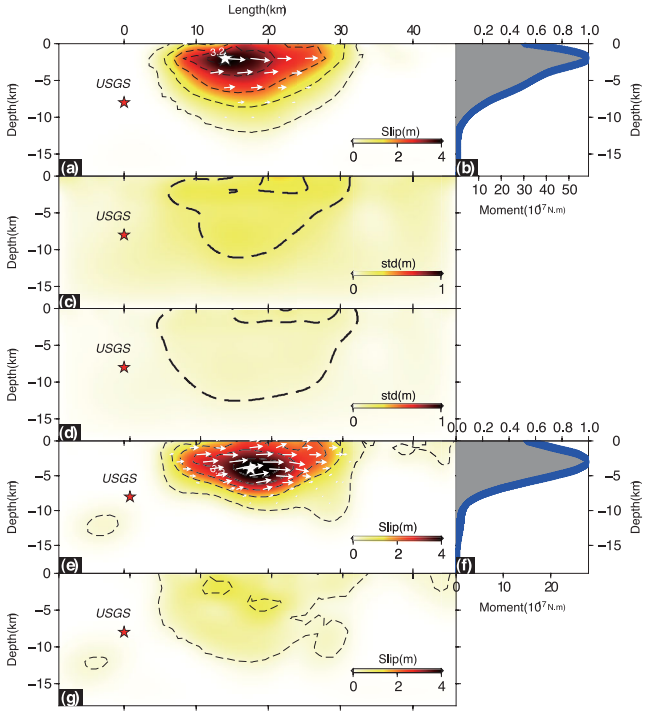

Figure 5. (a) Slip distribution (model A) of the 2011 Burma earthquake from both conventional InSAR and MAI observations. The red star represents the initial motion points determined by USGS and the white star gives the centroid (the area with a maximum slip) inferred from InSAR; (b) The grey area shows the sum of scalar moment release along strike and the blue line shows the normalized slip as the function of the depth. (c) and (d) are the standard deviations in slip along strike and down dip of the fault plane, respectively, from the Monte Carlo error analysis with 100 perturbed subsampled points. (e) is the slip distribution (model B) derived from two InSAR interferograms only and (f) is similar to (b) relative to the model (e). (g) The difference between model A and model B.

amplitude of ∼4.2 m at a depth of 2–4 km on a vertical, purely sinistral strike-slip rupture reaching to the surface. The total released moment is about 1.8×10^{19} N m (assuming a rigidity of 3.2×10^{10} Pa) and is equivalent to moment magnitude M_W 6.8. The major zone of slip is confined between the depths of 2–10 km, with a rupture length of ∼26 km. The maximum slip uncertainty reaches 0.5 m (Figs 5c and d), less than 10 per cent of the maximum rupture slip.

Fig. 5(e) shows the slip distribution determined using InSAR observations only (i.e. model B), and Fig. 5(g) shows the difference between model A and model B. It appears that the depth at which the major seismic moment was released drops ∼1.5 km from 2 km in model A to 3.5 km in model B, which is most likely due to the fact that MAI provided additional constraints in the near field where there was an absence of interferometric data.

Fig. 6 shows the simulated interferograms, AZI displacements and residuals from model A. The modelled interferograms can sufficiently explain InSAR observations with standard deviations of 1.6 and 1.4 cm for tracks 486 and 126, respectively. The RMS differences between SPO and modelled observations are 26 and 25 cm for tracks 126 and 486, respectively (Figs S7 and S8), while the RMS differences are ∼15 cm for both MAI maps. However, residuals of up to 5–6 cm can be observed close to the fault in Figs 6(c) and (f). One probable cause for these residuals in the near field is the slightly curved and stepping geometry of the real fault trace so that the simplified fault plane model fails to reproduce high fringe gradients close to the fault. Several previous InSAR studies have also reported that a simple elastic dislocation generally lacks the capability to model near-fault processes (e.g. Lohman & Simons 2005; Li *et al.* 2011). The maximum residual is located at the east end of the fault trace, where a small rupture segment with the amount of ∼0.2 m slip has been found in the slip distribution of model B. However, such a slip patch is not shown in model A, although there is a relatively big uncertainty in the same area (Fig. 5c). Note that landslides have been reported to have followed the main shock in this area, killing at least 10 people during the rupture (Vervaeck & Daniell 2011), which could partly explain the residual artefact. However, further evidence is required to fully support this point.

4 DISCUSSION

4.1 Coseismic slip deficit for strike-slip earthquakes

Coseismic slip deficits have been reported in several previous studies on slip distributions constrained with geodetic data for large strike-slip earthquakes (Fialko *et al.* 2002; Fialko 2004; Fialko *et al.* 2005; Kaneko & Fialko 2011), in other words, the inverted coseismic slip decreases towards the Earth surface. These studies suggested that inelastic deformation might be a major factor for the observed shallow slip deficits, which could introduce an 'artificial' deficit of up to 10 per cent of the maximum slip inferred from geodetic data.

A similar feature can also be observed in Fig. 5(a) and most of the seismic moment of the 2011 Burma earthquake was released at a depth of 4–5 km (Fig. 5b) along a 30-km-long left-lateral strike-slip rupture with a significant slip of ∼2 m near the surface, which reaches 50 per cent of the maximum amplitude of the inverted slip distribution. The frictional strength is one of the major factors to control the main rupture, and this strength should increase with depth (Das & Scholz 1983), which has been widely supported by *in situ* stress measurements (Mcgarr *et al.* 1982). In other words, the accumulated strain should also increase with depth before ruptures. Consequently, the increases in stress and/or strain with depth give two possible reasons why slip decreases towards the ground surface. Though our analysis cannot provide comprehensive understanding of the characteristics of slip in the uppermost crust, it is notable that the inverted slip distribution of the 2011 Burma earthquake shows similar features to several previous studies, summarized by Fialko *et al.* (2005).

4.2 Geomorphologic features

The NMF is one of the most active fault systems within the Burma region with an estimated slip rate of ∼3 mm yr^{-1} (Lacassin *et al.* 1998) based mainly upon large scale, long-term offset river bends. The fault segment that ruptured in the March 2011 event is likely to be the westward extension of the NMF (Fig. 7). Therefore, assuming a similar slip rate range and taking into account the average coseismic slip of about 3 m for the 2011 Burma earthquake, an earthquake recurrence interval of 1000–5000 yr is estimated for this segment for $M \sim 7$ events (assuming that this earthquake is characteristic in this region). This recurrence interval is much less than that along the plate boundaries, in particular the Sagaing fault where the earthquake recurrence interval of $M > 7$ is about 100–300 yr (Wang *et al.* 2011b). In terms of GPS measurements, the internal deformation in the Sunda plate is generally very small compared to the boundary

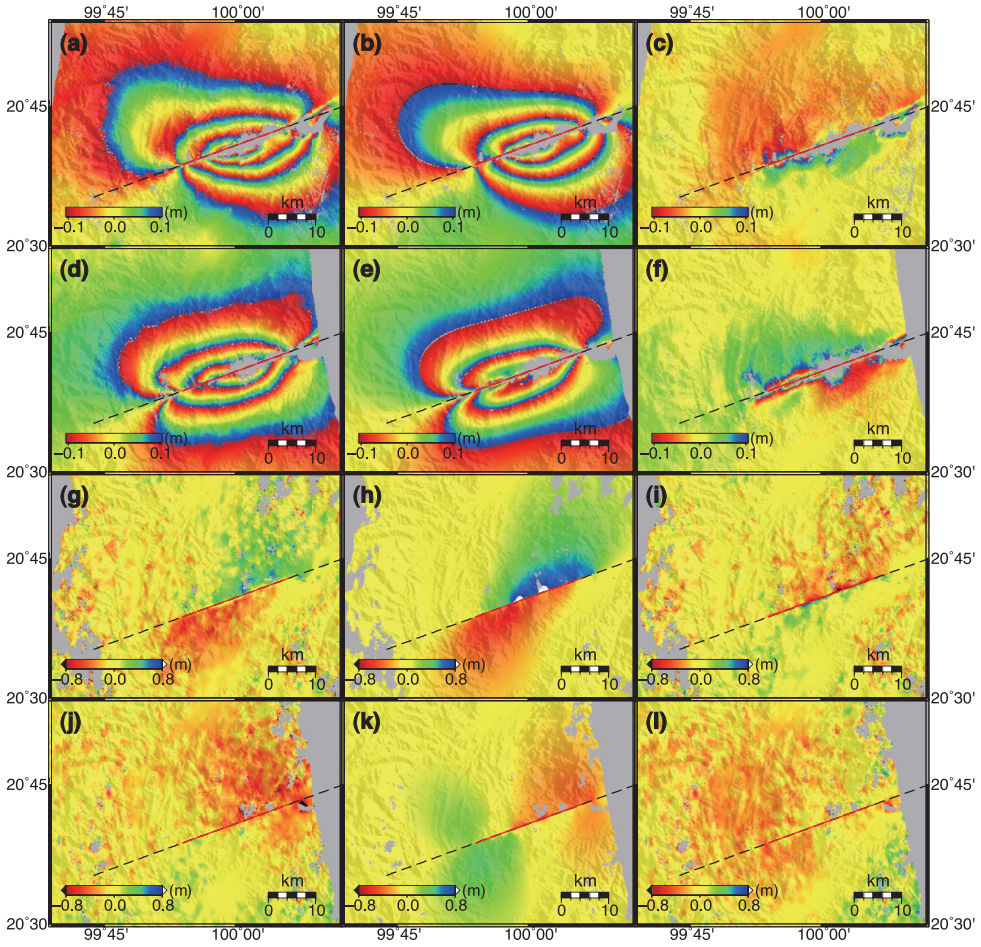

Figure 6. (a) Observations from track 126D, (b) modelled interferograms, (c) residuals (a minus b). (d), (e) and (f) are similar to (a), (b) and (c) but for track 486A. (g), (h) and (i) are MAI results for track 126D, and (j), (k) and (l) for track 486A. The red line marks the top boundary of the uniform model projected vertically to the surface, and the black dashed line is the 60-km-long model for the slip distribution.

of the plates (Simons *et al.* 2007), which is consistent with the basic knowledge to the NMF from local geomorphologic observations.

Hillshaded topography reveals a sinistrally offset ridge across the fault trace of the 2011 event (Fig. 7a). The offsets are of the order ∼3 km, recording the long-term fault displacement. Assuming a constant long-term slip rate equivalent to the NMF, this suggests that the fault activity started at least 1–5 Ma ago.

5 CONCLUSIONS

In this paper, we have demonstrated the key feature of SPO and MAI techniques: both can provide surface displacements in the along-track direction, and can be used to determine fault traces. We have also introduced a new statistic variable in a Log-function to simultaneously determine the optimal fault dip angle and smoothing factor when modelling slip distribution.

InSAR observations have been used to constrain the fault geometry of the 2011 March 24th Burma earthquake. Our optimal slip inversion for this large event indicates: (1) the rupture occurred on a vertical pure sinistral strike-slip fault with a strike of ∼70°; (2) the maximum slip is 4.2 m, occurring at a depth of 2.5 km; and (3) the total releasing moment is about 1.8×10^{19} N m, which is equal to a moment magnitude of 6.8. Our model suggests that the fault segment that ruptured in this event is likely to be the westward extension of the NMF (Fig. 7). However, this fault has not been identified in previous studies (Styron *et al.* 2010).

ACKNOWLEDGEMENTS

WF is supported by a China Scholarship Council (CSC) scholarship. This work was supported by the Natural Environmental Research Council (NERC) through the GAS project (Ref: NE/H001085/1), and the National Centre of Earth Observation (NCEO), of which the Centre for the Observation and Modeling of Earthquakes, Volcanoes and Tectonics (COMET+, http://comet.nerc.ac.uk) is a part. Part of this work was supported by National Natural Science Foundation of China (Project IDs: 41104028 and 41074005). We are grateful to JPL/Caltech for use of the ROI_PAC software. Most figures were made using the public domain Generic Mapping Tools (Wessel & Smith 1998). The ALOS data used in this study were shared by PIXEL (PALSAR Interferometry Consortium to Study our Evolving Land surface) and were provided from the Japan Aerospace Exploration Agency (JAXA) through a joint research contract between JAXA and the Earthquake Research Institute, University of Tokyo. The ownership of PALSAR data belongs to JAXA and Ministry of Economy, Trade and Industry of Japan. We are very grateful to the anonymous reviewers, and Editor Bert Vermeersen for thoughtful and thorough reviews that significantly improved this manuscript.

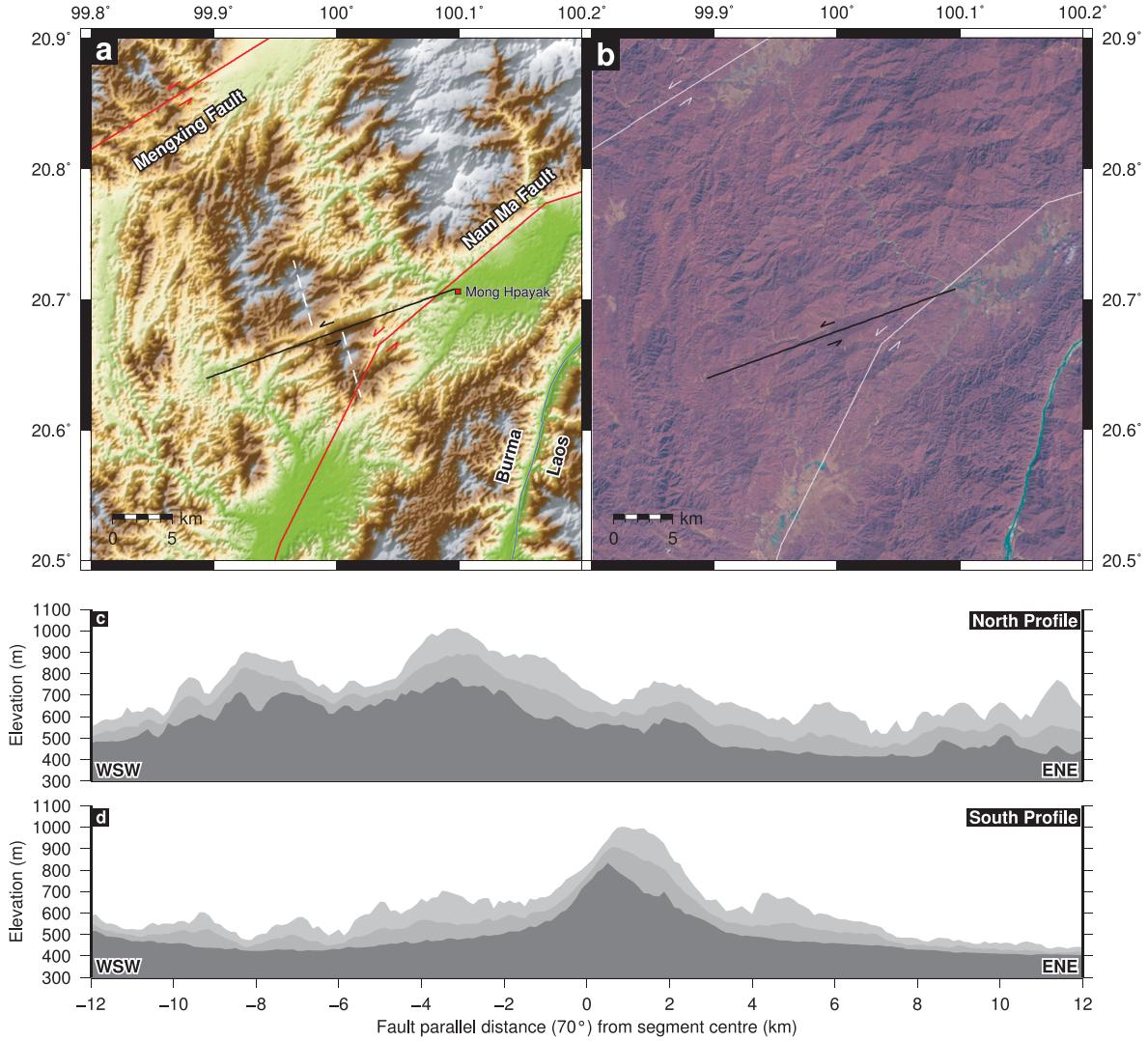

Figure 7. (a) SRTM 3-arc-second topography of the epicentral region of the 2011 earthquake. The fault trace from this study is delineated in black, previously mapped faults from Taylor & Yin (2009) in red. The fault segment here is likely the westward continuation of the NMF. Sinistrally offset north–south mountain ranges are visible in the topography as cut by the fault (white dashed lines mark their axes). (b) LANDSAT false colour image (RGB = 531). The region is densely vegetated, obscuring the fault geomorphology, but fault parallel drainage is clearly visible running along the same strike. (c) Fault parallel topographic swath profile (2 km wide showing maximum, mean and minimum elevations), 5 km north of the fault. (d) As for (c) but 5 km south of the profile, indicating the mountain ridges offset by 3 km across the fault.

REFERENCES

Atzori, S. *et al.*, 2009. Finite fault inversion of DInSAR coseismic displacement of the 2009 L'Aquila earthquake (Central Italy), *Geophys. Res. Lett.,* **36,** L15305, doi:10.1029/2009GL039293.

Barbot, S., Hamiel, Y. & Fialko, Y., 2008. Space geodetic investigation of the coseismic and postseismic deformation due to the 2003 Mw7.2 Altai earthquake: implications for the local lithospheric rheology, *J. geophys. Res.,* **113,** B03403, doi:10.1029/2007JB005063.

Bechor, N.B.D. & Zebker, H.A., 2006. Measuring two-dimensional movements using a single InSAR pair, *Geophys. Res. Lett.,* **33,** L16311, doi:10.1029/2006GL026883.

Ben-Dov, N.B. & Herring, T.A., 2011. Multiple aperture InSAR (MAI) with C-band and L-band: noise and precision, in *Proceedings of the ESA Fringe Workshop 2011,* Frascati, Italy.

Burgmann, R. *et al.*, 2002. Deformation during the 12 November 1999 Duzce, Turkey, earthquake, from GPS and InSAR data, *Bull. seism. Soc. Am.,* **92,** 161–171.

Chung, S.-L. *et al.*, 2005. Tibetan tectonic evolution inferred from spatial and temporal variations in post-collisional magmatism, *Earth-Sci. Rev.,* **65,** 173–196.

Daneill, J.E., Khazai, B., Wenzel, F. & Vervaeck, A., 2011. The CATDAT damaming earthquakes database, *Nat. Hazards Earth Syst. Sci.,* **11,** 2235–2251.

Das, S. & Scholz, C.H., 1983. Why large earthquakes do not nucleate at shallow depths, *Nature,* **305,** 621–623.

Feng, W., Xu, L., Xu, Z., Li, Z., Li, C. & Zhao, H., 2009. Source parameters of the 2008 Gerze Mw6.4 and Mw5.9 earthquakes from InSAR measurements, *Chin. J. Geophys.,* **52,** 983–993. (In Chinese with English Abstract.)

Feng, W.P. & Li, Z.H., 2010. A novel hybrid PSO/simplex algorithm for determining earthquake source paramers using InSAR data, *Progress Geophys.,* **25,** 1189–1196. (In Chinese.)

Fialko, Y., 2004. Probing the mechanical properties of seismically active crust with space geodesy: study of the co-seismic deformation due to the 1992 Mw7.3 Landers (southern California) earthquake, *J. geophys. Res.,* **109,** B03307, doi:10.1029/2003JB002756.

Fialko, Y., Sandwell, D., Agnew, D., Simons, M., Shearer, P. & Minster, B., 2002. Deformation on nearby faults induced by the 1999 Hector Mine Earthquake, *Science,* **297,** 1858–1862.

Fialko, Y., Sandwell, D., Simons, M. & Rosen, P., 2005. Three-dimensional deformation caused by the Bam, Iran, earthquake and the origin of shallow slip deficit, *Nature,* **435,** 295–299.

Fialko, Y., Simons, M. & Agnew, D., 2001. The complete (3-D) surface displacement field in the epicentral area of the 1999 Mw7.1 Hector Mine earthquake, California, from space geodetic observations, *Geophys. Res. Lett.,* **28,** 3063–3066.

Fukahata, Y. & Wright, T.J., 2008. A non-linear geodetic data inversion using ABIC for slip distribution on a fault with an unknown dip angle, *Geophys. J. Int*., **173,** 353–364.

Funning, G.J., Parsons, B., Wright, T.J., Jackson, J.A. & Fielding, E.J., 2005. Surface displacements and source paramenters of the 2003 Bam (Iran) earthquake from Envisat advanced synthetic aperture radar imagery, *J. geophys. Res.,* **110,** B09406, doi:10.1029/2004JB003338.

Goldstein, R.M. & Werner, C.L., 1998. Radar interferogram filtering for geophysical applications, *Geophys. Res. Lett.,* **25,** 4035–4038.

Goldstein, R.M., Zebker, H.A. & Werner, C.L., 1988. Satellite radar interferometry: two-dimensional phase unwrapping, *Radio Sci.,* **23,** 713–720.

Jarvis, A., Reuter, H.I., Nelson, A. & Guevara, E., 2008. Hole-filled SRTM for the globe version 4, available from the CGIAR-CSI SRTM 90 m database. Available at: http://srtm.csi.cgiar.org, last accessed 10 October 2011.

Jónsson, S., Zebker, H., Segall, P. & Amelung, F., 2002. Fault slip distribution of the 1999 Mw7.1 Hector Mine, California Earthquake, estimated from satellite radar and GPS measurements, *Bull. seism. Soc. Am.,* **92,** 1377–1389.

Jung, H.-S., Won, J.-S. & Kim, S.-W., 2009. An improvement of the performance of multiple-aperture SAR interferometry (MAI), *IEEE Trans. Geosci. Remote Sens.,* **47,** 2859–2869.

Kaneko, Y. & Fialko, Y., 2011. Shallow slip deficit due to larege strike-slip earthquakes in dynamic rupture simulations with elasto-plastic off-fault response, *Geophys. J. Int*., **186,** 1389–1403.

Lacassin, R., Replumaz, A. & Leloup, P.H., 1998. Hairpin river loops and slip-sense inversion on southeast Asian strike-slip faults, *Geology,* **26,** 703–706.

Li, Z., Elliott, J.R., Feng, W., Jackson, J.A., Parsons, B.E. & Walters, R.J., 2011. The 2010 Mw 6.8 Yushu (Qinghai, China) earthquake: constraints provided by InSAR and body wave seismology, *J. geophys. Res.,* **116,** B10302, doi:10.1029/2011JB008358.

Li, Z., Feng, W., Xu, Z., Cross, P. & Zhang, J., 2008. The 1998 Mw5.7 Zhangbei-Shangyi (China) earthquake revisited: a buried thrust fault revealed with interferomertic synthetic aperture radar, *Geochem. Geophys. Geosyst.,* **9,** Q04026, doi:10.1029/2007GC001910.

Lohman, R.B. & Simons, M., 2005. Some thoughts on the use of InSAR data to constrain models of surface deformation: noise structure and data downsampling, *Geochem. Geophys. Geosyst.,* **6,** Q01007, doi:10.1029/2004GC000841.

Marcotte, D., 1996. Fast variogram computation with FFT, *Comput. Geosci.,* **22,** 1175–1186.

Maung, H., 1987. Transcurrent movements in the Burma-Andaman Sea region, *Geology,* **15,** 911–912.

Maurin, T., Masson, F., Rangin, C., Min, U.T. & Collard, P., 2010. First global positioning system results in northern Myanmar: constant and localized slip rate along the Sagaing fault, *Geology,* **38,** 591–594.

Mcgarr, A., Zoback, M.D. & Hanks, T.C., 1982. Implications of an elastic analysis of in situ stress measurements near the San Andreas fault, *J. geophys. Res.,* **87,** 7797–7806.

Michel, R., Avonac, J.-P. & Taboury, J., 1999. Measuring ground displacements from SAR amplitude images: application to the Landers earthquake, *Geophys. Res. Lett.,* **26,** 875–878.

Molnar, P. & Tapponnier, P., 1975. Cenozoic tectonics of Asia: effects of a continental collision, *Science,* **189,** 419–426.

Okada, Y., 1985. Surface deformation due to shear and tensile faults in a half-space, *Bull. seism. Soc. Am.,* **75,** 1135–1154.

Parsons, B.E. *et al.*, 2006. The 1994 Sefidabeh (eastern Iran) earthquakes revisited: new evidence from satellite radar interferometry and carbonate dating about the growth of an active fold above a blind thrust fault, *Geophys. J. Int.,* **164,** 202–217.

Pathier, E., Fielding, E.J., Wright, T.J., Walker, R., Parsons, B.E. & Hensley, S., 2006. Displacement field and slip distribution of the 2005 Kashmir earthquake from SAR imagery, *Geophys. Res. Lett.,* **33,** L20310, doi:10.1029/2006GL027193.

Replumaz, A., Lacassin, R., Tapponnier, P. & Leloup, P.H., 2001. Large river offsets and Plio-Quaternary dextral slip rate on the Red River Fault (Yunnan, China), *J. geophys. Res.,* **106,** 819–836.

Rosen, P.A., Hensley, S., Peltzer, G. & Simons, M., 2004. Update repeat orbit interferometry package released, *EOS, Trans. Am. geophys. Un.,* **85,** 47.

Scharer, U., Tapponnier, P., Lacassin, R., Leloup, P.H., Dalai, Z. & Shaocheng, J., 1990. Intraplate tectonics in Asia: a precise age for large-scale miocene movement along the Ailao Shan-Red River shear zone, China, *Earth planet. Sci. Lett.,* **97,** 65–77.

Shen, Z.-K., Lu, J., Wang, M. & Burgmann, R., 2005. Contemporary crustal deformation around the southeast borderland of the Tibetan Plateau, *J. geophys. Res.,* **110,** B11409, doi:10.1029/2004JB003421.

Simons, M., Fialko, Y. & Rivera, L., 2002. Coseismic deformation from the 1999 Mw 7.1 Hector Mine, California, earthquake as inferred from InSAR and GPS observations, *Bull. seism. Soc. Am.,* **92,** 1390–1402.

Simons, W.J.F. *et al.*, 2007. A decade of GPS in Southeast Asia: resolving Sundaland motion and boundaries, *J. geophys. Res.,* **112,** B06420, doi:10.1029/2005JB003868.

Socquet, A., Vigny, C., Chamot-Rooke, N., Simons, W., Rangin, C. & Ambrosius, B., 2006. India and Sunda plates motion and deformation along their boundary in Myanmar determined by GPS, *J. geophys. Res.,* **111,** B05406, doi:10.1029/2005JB003877.

Stark, P.B. & Parker, R.L., 1992. Bounded-variable least-squares: an algorithm and applicatins, *Comput. Stat.,* **10,** 129–141.

Styron, R., Taylor, M. & Okoronkwo, K., 2010. Database of active structures from the Indo-Asian collision, *EOS, Trans. Am. geophys. Un.,* **91,** 181–188.

Sun, J., Shen, Z., Xu, X. & Bürgmann, R., 2008. Synthetic normal faulting of the 9 January 2008 Nima (Tibet) earthquake from conventional and along-track SAR interferometry, *Geophys. Res. Lett.,* **35,** L22308, doi:10.1029/2008gl035691.

Tapponnier, P. & Molnar, P., 1976. Slip-line field theory and large-scale continental tectonics, *Nature,* **264,** 319–324.

Taylor, M. & Yin, A., 2009. Active structures of the Himalayan-Tibetan orogen and their relationships to earthquake distribution, contemporary strain field, and Cenozoic volcanism, *Geosphere,* **5,** 199–214.

Trisirisatayawong, I., Hooper, A. & Aobpaet, A., 2011. Co-seismic displacement of 24-March-2011 Mw = 6.8 Mong Hpayak (Tarlay) Earthquake, Myanmar, in *Proceedings FRINGE Workshop ESA SP-697,* Frascati, Italy.

Vervaeck, A. & Daniell, J., 2011. Deadly earthquake in the border area of Myanmar, Thailand and Laos. Available at: http://earthquake-report.com/2011/03/26/massive-and-extremely-dangerous-earthquake-in-the-border-area-in-between-myanmar-thailand-laos-and-china/, last accessed 14 October 2011.

Vigny, C., Socquet, A., Rangin, C., Chamot-Rooke, N., Pubellier, M., Bouin, M.-N., Bertrand, G. & Becker, M., 2003. Present-day crustal deformation around Sagaing fault, Myanmar, *J. geophys. Res.,* **108,** 2533, doi:10.1029/2002jb001999.

Wang, H., Liu, M., Cao, J., Shen, X. & Zhang, G., 2011a. Slip rates and seismic moment deficits on major active faults in mainland China, *J. geophys. Res.,* **116,** B02405, doi:10.1029/2010JB007821.

Wang, Y., Sieh, K., Aung, T., Min, S., Khaing, S.N. & Tun, S.T., 2011b. Earthquakes and slip rate of the southern Sagaing fault: insights from an offset ancient fort wall, lower Burma (Myanmar), *Geophys. J. Int.,* **185,** 49–64.

Wessel, P. & Smith, W.H.F., 1998. New, improved version of generic mapping tools released, *EOS, Trans. Am. geophys. Un.,* **79,** 579.

Wright, T.J., Lu, Z. & Wicks, C., 2003. Source model for the Mw6.7, 23 October 2002, Nenana Mountain Earthquake (Alaska) from InSAR, *Geophys. Res. Lett.,* **30,** 1974, doi:10.1029/2003GL018014.

Yin, A., 2000. Mode of Cenozoic east-west extension in Tibet suggesting a common origin of rifts in Asia during the Indo-Asian collision, *J. geophys. Res.,* **105,** 21 745–21 759.

SUPPORTING INFORMATION

Additional Supporting Information may be found in the online version of this article:

Figure S1. (a) A trade-off curve line associated with the model with a dip angle of 87.3°. The thick and thin dashed black lines show the trends of model roughness and the residuals of modelled simulations after normalizing ($[\xi, \psi]$), respectively, while the solid grey line represents $\log(\xi + \psi)$. (b) Contour map of $\log(\xi + \psi)$ with variations of dips and hyperparameters (α^2). White star indicates the point of global minimum.

Figure S2. (a) The simulated slip model with a magnitude of 6.5. (b) The optimal slip model determined with subsampled displacements using the PSOKINV package.

Figure S3. 3-D surface displacements: (a) easting component; (b) northing component and (c) UP component.

Figure S4. (a) Track 126D: conventional interferogram; (b) far-field data of (a); (c) 2-D variogram calculated using all the valid pixels in the far-field as shown in (b). (d), (e) and (f) are similar to (a), (b) and (c) but for track 486A.

Figure S5. (a) and (c) azimuth offset map and along-track interferogram for track 126D, (b) and (d) are similar to (a) and (c), but for track 486A. (e), (f), (g) and (h) are corrected versions of (a), (b), (c) and (d) after removing a two-order best-fitting polynomial surface. Note: Only data in the non-deforming area as defined in Fig. S4 were used to estimate the best-fitting polynomial surface.

Figure S6. Resampled datapoints from: (a) track 126D interferogram, (b) track 486A interferogram, (c) track 126D MAI and (d) track 486A MAI. Note: the resolution-based (R-based) method proposed by Lohman & Simons (2005) was employed in this study.

Figure S7. (a) Range change from track 126D, (b) modelled range change, (c) residuals of (a minus b), while (d), (e) and (f) for azimuth offsets in the same track as (a), (b) and (c). (g), (h) and (i) are similar to (a), (b) and (c) but for range changes from track 486A, and (j), (k) and (l) are similar to (d), (e) and (f) but for azimuth offsets from track 486A. The red lines mark the surface projection of the top boundary of the uniform model and the black dashed line indicates the 60-km-long model for the slip distribution.

Figure S8. (a), (c) and (e) Comparisons of the NNE-SSW profiles of A−A′, B−B′ and C−C′ from track 126 as shown in Fig. 2(b), (d) and (f) are similar to (a), (c) and (e) but for track 486A. Green diamonds denote the SPO range offsets, blue triangles imply the conventional InSAR displacements and dashed red lines represent the modelled measurements. The grey-shaded region indicates topography along each profile, and the white lines down to the *x*-axis shows the location of the seismic fault.

Figure S9. Trade-off curve lines between model roughness and residuals (root mean square, RMS).

Figure S10. Uncertainties and trade-offs of single fault model parameters computed using Monte Carlo analysis. Scatterplots show degrees trade-off between pairs of model parameters, and the red triangle implies the best-fit solution for the uniform model as listed in Table 2. Histograms show the uncertainty in individual model parameter. μ and ξ are the mean and standard deviation of the distribution of each parameter with a 95 per cent confidential interval, respectively.

Table S1. Comparison of the geometry parameters between the Burma slip model and numerical experiment model (http://gji.oxfordjournals.org/lookup/suppl/doi:10.1093/gji/ggt254/-/DC1).

Please note: Oxford University Press are not responsible for the content or functionality of any supporting materials supplied by the authors. Any queries (other than missing material) should be directed to the corresponding author for the article.